Unidirectional reflectionless anti-parity-time-symmetric photonic lattices of thermal atoms

Yanyan He, Jinze Wu, Yaodong Hu, Jun-Xiang Zhang, and Shi-Yao Zhu
Interdisciplinary Center for Quantum Information and Zhejiang Province Key Laboratory of Quantum Technology and Device, Department of Physics, Zhejiang University, Hangzhou 310027, Zhejiang Province, China

(Received 4 October 2021; revised 19 February 2022; accepted 29 March 2022; published 18 April 2022)

We experimentally demonstrate an anti-parity-time (anti-PT)-symmetric photonic lattice in thermal cesium atoms driven by two standing-wave laser fields. Such a lattice possesses anti-PT-symmetric susceptibility, of which the real (imaginary) part is an odd (even) function of position. By manipulating the intensities and phases of the two standing-wave fields, we experimentally observe unidirectional reflectionless propagation at the exceptional points. Our work provides a platform to study the scattering property of anti-PT-symmetric systems.

DOI: 10.1103/PhysRevA.105.043712

I. INTRODUCTION

Parity-time (PT)-symmetric optical systems have triggered extensive research interest because of their novel properties and applications [1–10]. These systems are non-Hermitian and invariant under combined parity (P) and time-reversal (T) operations. Generally, they can be divided into two categories, i.e., coupled and scattering systems. For a PT-symmetric coupled system, the Hamiltonian $\hat{H}$ commutes with the combined parity-time operator $\hat{P}\hat{T}$, i.e., $[\hat{H}, \hat{P}\hat{T}] = 0$. A model system consists of a pair of coupled waveguides with gain in one waveguide and an equal amount of loss in the other [5]. PT-symmetric scattering systems demand balanced gain-loss modulation along the longitudinal direction z of light propagation, and the refractive indices satisfy $n(z) = n^*(-z)$. These systems include periodic Bragg structures [10,11] and photonic heterostructures [12,13] and have been extended to acoustic media [14–17]. In a PT-symmetric scattering system, the scattering matrix $\hat{S}$, which relates the output field to the input field, satisfies the relation $\hat{P}\hat{T}\hat{S}\hat{P}\hat{T} = \hat{S}^{-1}$ [12,13]. A common feature of the two systems is the phase-transition point, also called the exceptional point (EP), where not only the eigenvalues but also the corresponding eigenvectors of $\hat{H}$ or $\hat{S}$ become the same. It has led to many novel applications, such as sensing [18–23], directional lasing [24], asymmetric mode switching [25], and topological energy transfer [26]. EPs can give rise to unidirectional invisibility [6,10], which has been demonstrated in PT-symmetric scattering systems, such as passive PT-symmetric metamaterials [11], photonic lattices [6], and acoustics [15,16].

As a counterpart, anti-PT symmetry has attracted increasing attention recently. There are also two classes of systems associated with anti-PT symmetry. For an anti-PT-symmetric coupled system, the Hamiltonian anticommutes with the operator $\hat{P}\hat{T}$, i.e., $\{\hat{H}, \hat{P}\hat{T}\} = 0$ [27–41]. This anticommutation relationship reveals that anti-PT-symmetric systems do not necessarily need gain to explore non-Hermitian dynamics and can display distinct properties, such as constant refraction [27], coherent switch [29], and energy-difference conservation [31,41]. Contrary to PT-symmetric scattering systems, an anti-PT-symmetric scattering system requires the refractive index to satisfy $n(z) = -n^*(-z)$ [42], which needs balanced positive- and negative-refractive-index materials.

However, the realization of this scattering system may encounter difficulties in arranging negative-refractive-index materials. Wu *et al.* [43,44] proposed another kind of anti-PT-symmetric scattering system, in which the spatial susceptibility rather than the refractive index is antisymmetric under the combined PT operations, i.e., $\chi(z) = -\chi^*(-z)$. Such an anti-PT-symmetric scattering system requires neither optical gain nor a negative refractive index. Nevertheless, it can realize unidirectional reflectionless light propagation at the EP. Despite several subsequent proposals [45–47] in cold atoms, the experimental demonstration has not been achieved yet.

On the other hand, based on the well-known effect of electromagnetically induced transparency (EIT) [48], thermal atomic media provide a flexible platform for realizing controllable photonic lattices (so-called Bragg gratings) [49–54] through periodically modulating the dispersion and absorption using standing-wave coupling fields. Recently, one-dimensional (1D) PT-symmetric optical lattices with periodic gain and loss profiles were demonstrated in an atomic medium [55]. In particular, asymmetric reflection due to momentum-space chiral edge currents was observed in thermal atoms [56]. Here we show that based on such a system we can realize anti-PT-symmetric photonic lattices in real space.

We use one weak probe field and two standing-wave (coupling and modulating) fields to drive Λ-type atoms, forming a 1D photonic lattice along the propagation direction of the probe field. The anti-PT-symmetric susceptibility for the probe field is achieved by fixing the spatial phase difference ϕ between the two standing-wave fields at $\pi/2$ or $3\pi/2$. By modulating the real and imaginary parts of the probe susceptibility through the two standing-wave fields, we observe unidirectional reflectionless propagation at the EP of

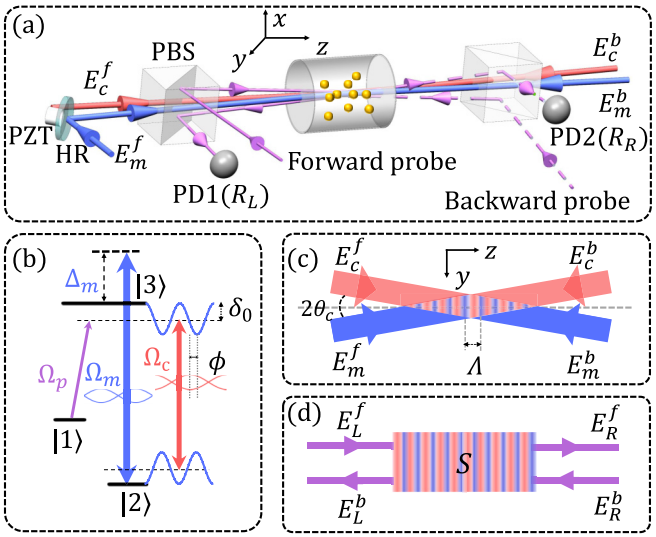

FIG. 1. (a) Experimental setup. The forward (E_c^f) and backward (E_c^b) beams from the same laser form the standing-wave coupling field in the vapor cell. Similarly, the forward (E_m^f) and backward (E_m^b) beams from a second laser form the standing-wave modulating field. The forward (purple solid line) and backward (purple dashed line) probe beams transmit through the lattice from the left and right sides of the vapor cell, respectively. The 5-cm-long vapor cell is wrapped with μ-metal sheets to shield magnetic fields. PD1 and PD2: photodetectors, PBS: polarizing beam splitter, HR: high-reflectivity mirror, PZT: piezoelectric ceramic. (b) The Λ-type energy levels of ^{133}Cs atoms. The far-detuned standing-wave modulating field Ω_m induces periodic ac Stark shifts (blue curves) on levels $|2\rangle$ and $|3\rangle$. The coupling field is resonant with the transition between shifted levels when the modulating field exists. (c) The spatial arrangement of the coupling [red (light gray)] and modulating [blue (dark gray)] fields inside the vapor cell. (d) The scattering process on the lattice. Input fields (E_L^f, E_R^b) are scattered into two output fields (E_L^b, E_R^f), which is described by the scattering matrix S.

the anti-PT-symmetric photonic lattice. Our work not only demonstrates anti-PT symmetry in a 1D scattering system but also provides a class of synthetic non-Hermitian lattices for controlling light propagation [11,57–59].

This paper is organized as follows. In Sec. II we introduce the experimental setup implemented in a Λ-type atomic system and derive the spatial susceptibility for the probe field. In Sec. III we show the construction of the anti-PT-symmetric photonic lattice in this atomic system. In Sec. IV we discuss the phase transition of the scattering matrix. The unidirectional reflectionless propagation is related to the phase-transition point, i.e., the EP. In addition, an exceptional line is predicted in this system. In Sec. V we show experimental observations of the unidirectional reflectionless propagation and the exceptional line, and our conclusion is presented in Sec. VI.

II. EXPERIMENTAL SETUP

The experimental setup is schematically depicted in Fig. 1(a). Two standing-wave laser fields and one probe laser field are coupled to Λ-type ^{133}Cs atoms [see Fig. 1(b)], which have two ground states, $|2\rangle = |6S_{1/2}, F = 3\rangle$ and $|1\rangle = |6S_{1/2}, F = 4\rangle$, and one excited state, $|3\rangle = |6P_{1/2}, F = 4\rangle$. The decay rate of the excited state is $\Gamma = 2\pi \times 4.6$ MHz, and the frequency difference between the two ground states is $2\pi \times 9.2$ GHz. The probe field (frequency ω_p, wavelength λ_p, Rabi frequency Ω_p) couples the transition $|1\rangle \leftrightarrow |3\rangle$, while the transition $|2\rangle \leftrightarrow |3\rangle$ is driven by two standing-wave fields. One of the standing-wave fields is nearly resonant with the transition (called the coupling field), while the other is far detuned from the transition (called the modulating field). Two counterpropagating coupling beams, E_c^f and E_c^b (ω_c, λ_c, Ω_c), from the same external cavity diode laser intersect at the center of the vapor cell at an angle $\theta_c \approx 0.42^\circ$ with respect to the z axis [see Fig. 1(c)]. These two beams generate a standing wave along the z direction and form the standing-wave coupling field. The Rabi frequency envelope can be written as $2\Omega_c \cos(k_c z)$, where k_c is the z component of the wave vector. The coupling field induces a spatially periodical modulation of absorption under the EIT condition, i.e., $\Delta_c = \Delta_p = 0$, where $\Delta_c = \omega_c - \omega_{32}$ and $\Delta_p = \omega_p - \omega_{31}$ are the frequency detunings of coupling and probe fields, with ω_{ij} being the atomic transition frequency between $|i\rangle$ and $|j\rangle$. In this case, a 1D photonic lattice with periodic absorption modulation along the z direction is generated.

Two counterpropagating modulating beams, E_m^f and E_m^b (ω_m, λ_m, Ω_m), from a second external cavity diode laser overlap with E_c^b and E_c^f, respectively [see Fig. 1(c)]. They form the standing-wave modulating field with the Rabi frequency envelope $2\Omega_m \cos(k_m + \phi/2)$, where $k_m \approx k_c$ is the z component of the wave vector and $\phi/2$ is the spatial phase difference between these two standing-wave fields. The phase can be tuned by a piezoelectric ceramic attached to a mirror [see Fig. 1(a)]. The far-detuned standing-wave modulating field induces dispersion modulation on the lattice through a spatially periodic ac Stark shift $\delta(z, \phi) = \delta_0 \cos(2k_m z + \phi) + \delta_0$, where $\delta_0 = 2\Omega_m^2/\Delta_m$ is the spatially homogeneous Stark shift, with $\Delta_m = \omega_m - \omega_{32}$ being the frequency detuning and $\Delta_m \gg \Omega_m$ [see Fig. 1(b)]. Therefore, a 1D complex photonic lattice with modulations of the dispersion and absorption is generated in the vapor cell. The period of the lattice is $\Lambda = \lambda_c/[2\cos\theta_c]$.

When two weak probe beams enter the lattice from the left (forward) and right (backward) sides, they experience spatially periodic modulations of the dispersion and absorption, and first-order Bragg ($\lambda_p \approx 2\Lambda$) reflected fields are generated and detected by two photodetectors (PDs) [see Fig. 1(a)]. The two probe beams are aligned parallel with a small distance between them so that they do not interfere. In the experiment, the e^{-2} full widths of the coupling and modulating beams are both 2.5 mm. The e^{-2} full widths of the probe beams are 0.9 mm, and they are fully covered by the two standing-wave beams in the vapor cell.

Under the rotating-wave approximation, the effective Hamiltonian of the system in a rotating frame is

$$\begin{aligned} H_{\text{eff}}/\hbar = &-\Omega_p e^{ik_p z}|3\rangle\langle 1| - 2\Omega_c \cos(k_c z)|3\rangle\langle 2| \\ &+ [\delta_0 \cos(2k_m z + \phi) + \delta_0 - \Delta_{pc}]|2\rangle\langle 2| \\ &- [\delta_0 \cos(2k_m z + \phi) + \delta_0 + \Delta_p]|3\rangle\langle 3| + \text{H.c.}, \quad (1) \end{aligned}$$

where $\Delta_{pc} = \Delta_p - \Delta_c$ is the two-photon detuning. The third and fourth terms are the ac Stark shifts $\pm[\delta_0 \cos(2k_m z + \phi) +$

δ_0] induced by the modulating field on levels $|2\rangle$ and $|3\rangle$, respectively [see Fig. 1(b)].

The spatial susceptibility χ for the probe field can be obtained through the standard density-matrix formalism (see Appendix A). Due to the thermal atomic motion in the system, the susceptibility at position z is contributed by atoms with different velocities v,

$$\chi(z) = \frac{\mathcal{N}|\mu_{31}|^2}{\epsilon_0 \hbar \Omega_p} \sum_{n=-\infty}^{+\infty} e^{-2ink_c z} \int_{-\infty}^{+\infty} f(v)\rho_{31}^{[n]}(v)dv, \quad (2)$$

where $\rho_{31}^{[n]}(v)$ is the Fourier coefficient of the density matrix, $\mathcal{N}$ is the atomic density, μ_{31} is the relevant dipole moment of transition $|1\rangle \leftrightarrow |3\rangle$, ϵ_0 is the permittivity in vacuum, and $f(v) = e^{-v^2/u^2}/\sqrt{\pi}u$ is Maxwell's velocity distribution function, with u being the most probable speed. The real (Reχ) and imaginary (Imχ) parts of the susceptibility represent the spatial dispersion and absorption of the lattice, respectively. The effect of the thermal atomic motion on the spatial susceptibility is discussed in Appendix C.

III. ANTI-*PT*-SYMMETRIC PHOTONIC LATTICES

In the experiment, the detuning and Rabi frequency of the modulating field are $\Delta_m = 50\Gamma$ and $\Omega_m = 6.67\Gamma$, so the spatially homogeneous Stark shift $\delta_0 = 2\Omega_m^2/\Delta_m = 1.78\Gamma$. Figures 2(a) and 2(b) show the calculated spatial susceptibilities with $\Delta_p = -\delta_0$ for $\phi = \pi/2$ and $\phi = 3\pi/2$, respectively. At these two phases, Reχ (Imχ) is an odd (even) function of position, indicating that an anti-*PT*-symmetric lattice $\chi(z) = -\chi^*(-z)$ can be established in such an atomic configuration. The period and position of the lattice are determined by the standing-wave pattern. Here the $z = 0$ point is defined at one of the nodes of the standing-wave coupling field, and it does not affect the anti-*PT* symmetry of the lattice (see Appendix C). We discuss the influence of two standing-wave fields on the lattice in three cases, namely, with both standing-wave fields, with only the coupling field, and with only the modulating field. We find that when both fields exist, Reχ (Imχ) almost overlaps with that when only the modulating (coupling) field exists. This means that the spatial absorption (dispersion) modulation of the lattice is mainly determined by the coupling (modulating) field. The phase ϕ determines the spatial phase difference between Reχ and Imχ of the lattice, which exhibits its advantage in constructing reconfigurable and tunable non-Hermitian lattices.

The spatial susceptibility that governs the first-order Bragg reflection of the probe field on the lattice can be written as [43,44]

$$\chi \approx i\chi_{i0} + \chi_{r0} + i\chi_i \cos(2k_c z) + \chi_r \cos(2k_m z + \phi), \quad (3)$$

where χ_{i0}, χ_{r0}, χ_i, and χ_r are the positive Fourier coefficients and can be numerically calculated (see Appendix B). χ_{i0} and χ_{r0} are the constant background absorption and dispersion coefficients, respectively. χ_i and χ_r are the modulation amplitudes of the absorption and dispersion, respectively.

The modulation amplitudes χ_i and χ_r can be tuned by the coupling and modulating fields. Figure 2(c) shows χ_i and χ_r versus Ω_c and Ω_m^2/Δ_m for $\phi = \pi/2$. There are two surfaces, $\chi_i(\Omega_c, \Omega_m^2/\Delta_m)$ and $\chi_r(\Omega_c, \Omega_m^2/\Delta_m)$, in the parameter space

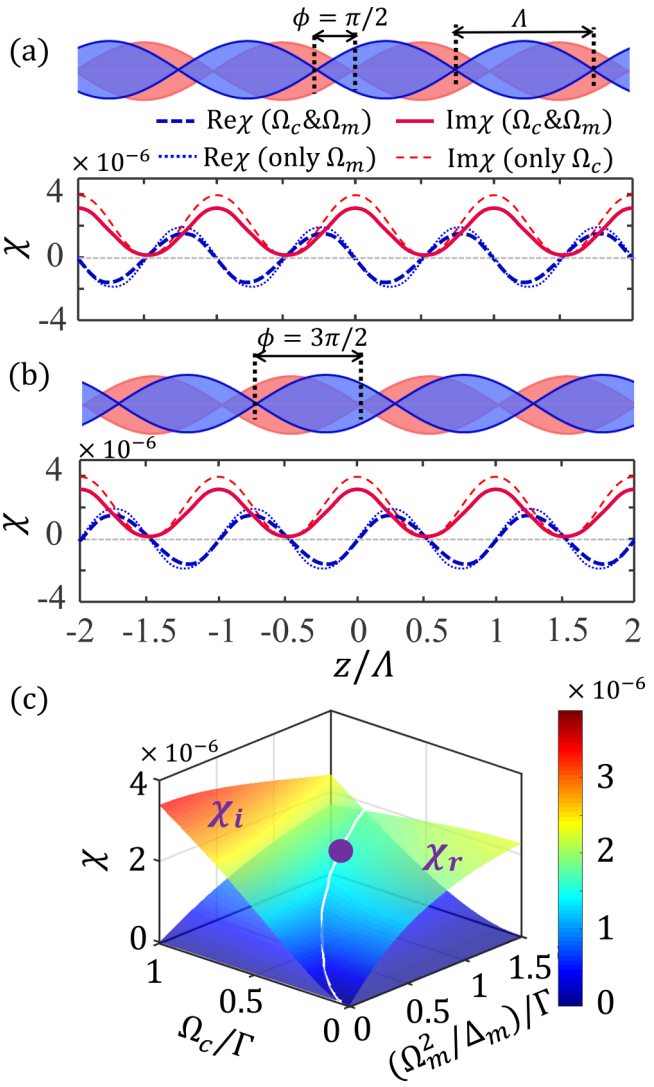

FIG. 2. The spatial susceptibilities for (a) $\phi = \pi/2$ and (b) $\phi = 3\pi/2$. The top panels in (a) and (b) show the relative position of the standing-wave coupling-field (red back) and modulating-field (blue front) envelopes. The bottom panels in (a) and (b) show the corresponding spatial susceptibilities in three cases. (i) When both standing-wave fields exist, Reχ is represented by the thick blue dashed lines, and Imχ is represented by the red solid lines. (ii) When only the coupling field exists, Imχ is represented by the thin red dashed lines. (iii) When only the modulating field exists, Reχ is denoted by the blue dotted lines. The parameters are as follows: (i) $\Omega_c = 0.65\Gamma$, $\Omega_m = 6.67\Gamma$, $\Delta_m = 50\Gamma$, $\delta_0 = 1.78\Gamma$, $\Delta_c = -2\delta_0 = -3.56\Gamma$, and $\Delta_p = -\delta_0 = -1.78\Gamma$; (ii) $\Omega_c = 0.65\Gamma$, $\Omega_m = 0$, $\Delta_c = 0$, and $\Delta_p = 0$; and (iii) $\Omega_c = 0$, $\Omega_m = 6.67\Gamma$, $\Delta_m = 50\Gamma$, $\delta_0 = 1.78\Gamma$, $\Delta_c = 0$, and $\Delta_p = -\delta_0 = -1.78\Gamma$. (c) Modulation amplitudes of dispersion (χ_r) and absorption (χ_i) versus Ω_c and Ω_m^2/Δ_m for $\phi = \pi/2$. The detunings are $\Delta_p = -2\Omega_m^2/\Delta_m$ and $\Delta_c = -4\Omega_m^2/\Delta_m$. The violet dot in the intersection line represents one EP ($\Omega_c = 0.65\Gamma$, $\Omega_m^2/\Delta_m = 0.89\Gamma$).

$(\Omega_c, \Omega_m^2/\Delta_m)$, from which we can see that the dispersion χ_i and absorption χ_r mainly depend on Ω_c and Ω_m, respectively. χ_i (χ_r) increases with Ω_c (Ω_m) and changes little with Ω_m (Ω_c). The two surfaces of χ_i and χ_r have an intersection line where χ_i is equal to χ_r. As we will discuss below,

this line is responsible for the unidirectional reflectionless propagation.

IV. PHASE TRANSITION OF THE SCATTERING MATRIX

The anti-PT-symmetric lattice can be probed by the forward and backward probe fields, which are incident into the lattice from the left and right sides, respectively. The scattering on the lattice can be described by the scattering matrix S, which relates the output electric fields (E_L^b, E_R^f) to the input electric fields (E_R^b, E_L^f) [see Fig. 1(d)],

$$\begin{bmatrix} E_L^b \\ E_R^f \end{bmatrix} = \begin{bmatrix} t_R & r_L \\ r_R & t_L \end{bmatrix} \begin{bmatrix} E_R^b \\ E_L^f \end{bmatrix} = S \begin{bmatrix} E_R^b \\ E_L^f \end{bmatrix}, \tag{4}$$

where the subscript L (R) represents the fields on the left (right) side of the lattice and superscript f (b) denotes the forward (backward) fields. $r_{L(R)}$ and $t_{L(R)}$ are the reflection and transmission coefficients for incidence from the left (right). They can be analytically obtained by solving coupled-mode equations (see Appendix B). The scattering matrix of the anti-PT-symmetric lattice (at $\phi = \pi/2$) can be written as

$$S = \frac{1}{Z} \begin{bmatrix} \sqrt{4\chi_{i0}^2 - \chi_i^2 + \chi_r^2} & (\chi_r - \chi_i)\sinh(\xi L) \\ -(\chi_r + \chi_i)\sinh(\xi L) & \sqrt{4\chi_{i0}^2 - \chi_i^2 + \chi_r^2} \end{bmatrix}, \tag{5}$$

where $Z = \sqrt{4\chi_{i0}^2 - \chi_i^2 + \chi_r^2}\cos(\xi L) + 2\chi_{i0}\sinh(\xi L)$ and $\xi = (k_p/4n_0^2)\sqrt{4\chi_{i0}^2 - \chi_i^2 + \chi_r^2}$. L is the length of the lattice, and $n_0 = \sqrt{1+\chi_{r0}}$ is the background refractive index. Although the scattering matrix S is non-Hermitian ($S^\dagger \neq S$), it satisfies the pseudo-Hermitian condition $\eta^{-1} S \eta = S^\dagger$ [40,60], with $\eta = \sigma_x$ being the Pauli matrix.

The eigenvalues of S are given by

$$s_\pm = 4n_0^2\xi/(k_p Z) \pm \sinh(\xi L)\sqrt{\chi_i^2 - \chi_r^2}/Z, \tag{6}$$

which can be real or complex depending on the relation between χ_i and χ_r, tunable with Ω_c and Ω_m [see Fig. 2(c)]. In Figs. 3(a) and 3(b), we show $\mathrm{Re}s_\pm$ and $\mathrm{Im}s_\pm$ as functions of Ω_c and Ω_m^2/Δ_m. One specific case of $\Omega_m^2/\Delta_m = 0.89\Gamma$ [white lines in Figs. 3(a) and 3(b)] is highlighted in Figs. 3(c) and 3(d). From these plots, we can see that $s_\pm$ are complex-conjugate pairs $s_\pm = s_\mp^*$ when $\Omega_c < 0.65\Gamma$ ($\chi_i < \chi_r$). In contrast, $s_\pm$ are both real when $\Omega_c > 0.65\Gamma$ ($\chi_i > \chi_r$). The phase transition occurs at $\Omega_c = 0.65\Gamma$ ($\chi_i = \chi_r$) with $s_+ = s_-$, which indicates an EP. We define the EP as $\Omega_c^{\mathrm{EP}} = 0.65\Gamma$. At the EP, the reflection coefficients $r_L = 0$ and $r_R \neq 0$ [see Eq. (5)], which represent the unidirectional reflectionless propagation. From Figs. 3(a) and 3(b), we can see a line where $s_+ = s_-$. Each point on this line represents one EP. This line, therefore, is called an exceptional line.

The unidirectional reflectionless propagation can be understood from the wave-vector matching condition [17]. At $\phi = \pi/2$ and $\chi_i = \chi_r$, the modulation of the susceptibility is $\Delta\chi \sim i\chi_i\cos(2k_c z) - \chi_r\sin(2k_c z) = i\chi_i e^{2ik_c z}$, which offers a unidirectional wave vector $\mathbf{q} = 2k_c\hat{z}$ along the $+z$ axis. The wave-vector matching condition for the reflection on the lattice is $\mathbf{k_r} = \mathbf{k_p} + \mathbf{q}$, where $\mathbf{k_p}$ and $\mathbf{k_r}$ are the wave vectors of the incident probe field and the reflected field, respectively.

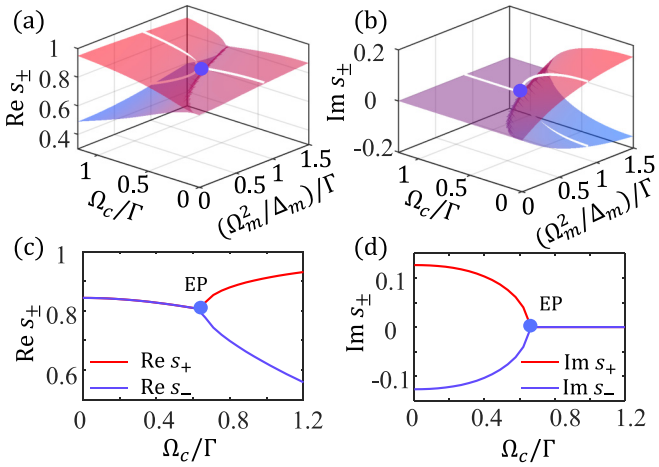

FIG. 3. The phase transition of the scattering matrix. (a) $\mathrm{Re}s_\pm$ and (b) $\mathrm{Im}s_\pm$ versus Ω_c and Ω_m^2/Δ_m. (c) $\mathrm{Re}s_\pm$ and (d) $\mathrm{Im}s_\pm$ versus Ω_c for $\Omega_m^2/\Delta_m = 0.89\Gamma$. EPs ($\Omega_c = 0.65\Gamma$, $\Omega_m^2/\Delta_m = 0.89\Gamma$) are marked by the blue dots. Other parameters are the same as in Fig. 2(c).

The wave-vector matching condition is satisfied only for the backward probe field with the wave vector $-k_p\hat{z}$, i.e., $\mathbf{k_r} = 2k_c\hat{z} - k_p\hat{z} \approx k_p\hat{z}$, giving rise to the unidirectional reflectionless propagation for the forward probe field ($r_L = 0$ and $r_R \neq 0$). In contrast, at $\phi = 3\pi/2$, the unidirectional wave vector is $\mathbf{q} = -2k_c\hat{z}$, which is along the $-z$ axis. In this case, the wave-vector matching condition is satisfied only for the forward probe field with the wave vector $k_p\hat{z}$, i.e., $\mathbf{k_r} = -2k_c\hat{z} + k_p\hat{z} \approx -k_p\hat{z}$, leading to the unidirectional reflectionless propagation for the backward probe field ($r_R = 0$ and $r_L \neq 0$). Therefore, we can adjust the phase ϕ to control the unidirectional wave vector to change the direction of unidirectional reflectionless propagation.

V. OBSERVATION OF THE UNIDIRECTIONAL REFLECTIONLESS PROPAGATION AT EPs

The reflection spectra in the two opposite directions are detected by two photodetectors, PD1 and PD2 [see Fig. 1(a)]. The reflection spectra for $\phi = \pi/2$ and $3\pi/2$ are shown in Figs. 4(a) and 4(b), respectively. We can see that the reflection spectra display a significant asymmetry. The reflectivity $R_L(= |r_L|^2) < R_R(= |r_R|^2)$ for $\phi = \pi/2$, while $R_L > R_R$ for $\phi = 3\pi/2$. Especially, we observe the fully unidirectional reflection at the probe detuning $\Delta_p = -\delta_0 = -1.78\Gamma$ [orange circles in Figs. 4(a) and 4(b)]. We can see that $R_L = 0$ for $\phi = \pi/2$, while $R_R = 0$ for $\phi = 3\pi/2$. Therefore, the unidirectional reflection indicates the existence of the anti-PT-symmetric photonic lattice in the vapor cell [see Figs. 2(a) and 2(b)]. The transmissivities are always equal, i.e., $T_L(= |t_L|^2) = T_R(= |t_R|^2)$ for any value of ϕ (not shown), indicating the optical reciprocity. The theoretical simulations of R_L and R_R are calculated using the transfer-matrix method [43,61]. The discrepancies between the experimental data and theoretical simulations result from Gaussian rather than plane-wave profiles of the laser fields, inhomogeneous profile of the lattice

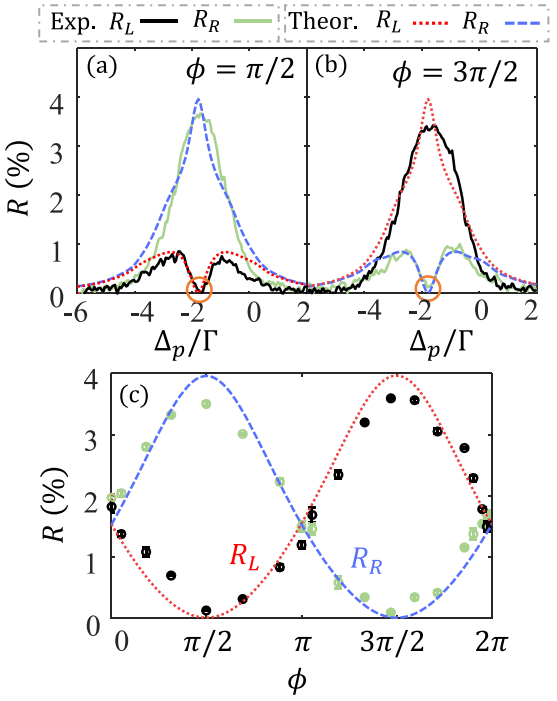

FIG. 4. Experimental data and theoretical simulations of reflection spectra for (a) $\phi = \pi/2$ and (b) $\phi = 3\pi/2$. The orange circles mark the unidirectional reflection at $\Delta_p = -\delta_0 = -1.78\Gamma$. (c) R_L and R_R versus ϕ for $\Delta_p = -1.78\Gamma$. The dots are experimental data for R_L (black dots) and R_R (green dots). The error bars are obtained by four independent measurements. The red dotted lines (blue dashed lines) are numerical simulations for R_L (R_R). Experimental parameters are $P_p = 20\ \mu$W, $P_c = 0.56$ mW, $P_m = 48$ mW, $\Delta_c = -3.56\Gamma$, $\Omega_m = 6.67\Gamma$, and $\Delta_m = 50\Gamma$. Theoretical parameters are $\Omega_c = 0.65\Gamma$, $\Delta_c = -3.56\Gamma$, $\Omega_m = 6.67\Gamma$, and $\Delta_m = 50\Gamma$. The weak reflectivity is due to the low power of the coupling field.

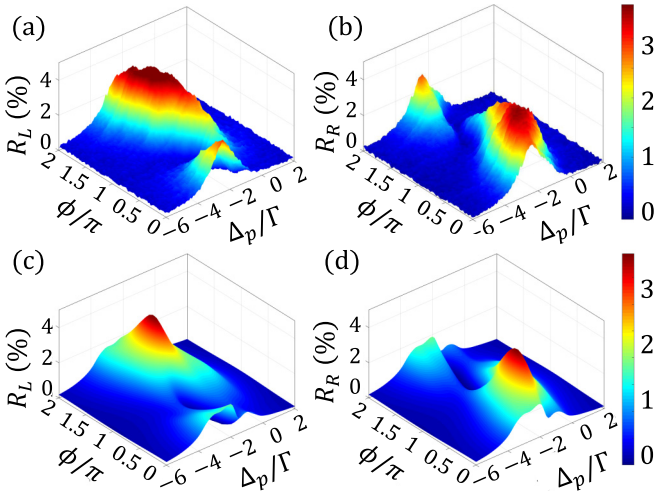

FIG. 5. Reflection spectra with different phases. (a) and (b) Experimental data. (c) and (d) Theoretical simulations. The experimental and theoretical parameters are the same as in Fig. 4.

[see Fig. 1(c)], the loss on the windows of the vapor cell, and asymmetric optical alignment.

To investigate the influence of ϕ on the reflections, we plot R_L and R_R versus ϕ for $\Delta_p = -1.78\Gamma$ in Fig. 4(c). We can see that R_L and R_R strongly depend on the phase ϕ. It is found that R_L and R_R satisfy the relation $R_L(\phi) = R_R(2\pi - \phi)$. The symmetric reflections ($R_L = R_R$) occur at only $\phi = 0$ and π. With the increase of ϕ from 0 to $\pi/2$, R_L decreases to zero, while R_R increases to the maximum. When ϕ increases from $\pi/2$ to π, R_L and R_R gradually become the same again. The fully unidirectional reflection can be realized when $\phi = \pi/2$ ($R_L = 0$) and $\phi = 3\pi/2$ ($R_R = 0$).

To further examine how the phase ϕ affects the reflections for $\Delta_p \neq -1.78\Gamma$, we plot the reflection spectra for different phases in Fig. 5. We see that the unidirectional reflection can be observed even when the phase ϕ is not exactly $\pi/2$ or $3\pi/2$, with a probe detuning Δ_p different from -1.78Γ. Therefore, we can obtain the unidirectional reflectionless propagation within a range of probe frequencies by tuning the phase ϕ.

Owing to the dependence of χ_i on Ω_c, the EP can be accessed by tuning Ω_c. When $\chi_i = \chi_r$, the anti-PT-symmetric lattice reaches an EP, where the unidirectional reflection can be observed. In Fig. 6(a), we plot the reflectivities R_L and R_R versus Ω_c for $\Delta_p = -1.78\Gamma$ at $\phi = \pi/2$. It is seen that R_L and R_R change in a different way when Ω_c is increased from 0 to 1.2Γ. When the coupling field is absent, i.e., $\Omega_c = 0$, we observe symmetric reflections ($R_L = R_R$). When we increase Ω_c, R_R increases gradually, while R_L first decreases and then increases. We observe $R_L = 0$ when $\Omega_c = 0.65\Gamma$, i.e., at the EP $\Omega_c^{\rm EP}$.

In Fig. 6(b), the dependence of $\Omega_c^{\rm EP}$ on Ω_m^2/Δ_m is plotted, where the theoretical line represents $\chi_i(\Omega_c, \Omega_m^2/\Delta_m) = \chi_r(\Omega_c, \Omega_m^2/\Delta_m)$, as shown by the white line in Fig. 2(c). It can be seen that the unidirectional reflection is observable on this line. Therefore, an exceptional line is achieved in this system. Furthermore, if more parameters that affect $\Omega_c^{\rm EP}$ are considered, we can realize high-dimensional EPs, such as an exceptional surface [62] and an exceptional volume.

VI. CONCLUSION

In conclusion, we have experimentally demonstrated an anti-PT-symmetric photonic lattice in a thermal atomic medium. This lattice is achieved by controlling the spatial phase difference ϕ between the standing-wave coupling and modulating fields. Unidirectional reflectionless light propagation, the key property of the anti-PT-symmetric photonic lattice, is observed at EPs. Thanks to the multiple tunable parameters in our system, an exceptional line is achieved in the experiment. The anti-PT-symmetric lattice can be extended to two-dimensional lattices and used to study other exotic effects, including coherent perfect absorption [63] and nonreciprocal diffraction [59,64]. We envision that our approach could be readily extended to the fields of acoustics [14–17], plasmonics, and photonics [1], and it provides a platform for non-Hermitian physics and potential applications [2], such as dynamically circling EPs [25,65], phase-dependent nonlinear dynamics, and quantum simulations using superradiance lattices [56,66].

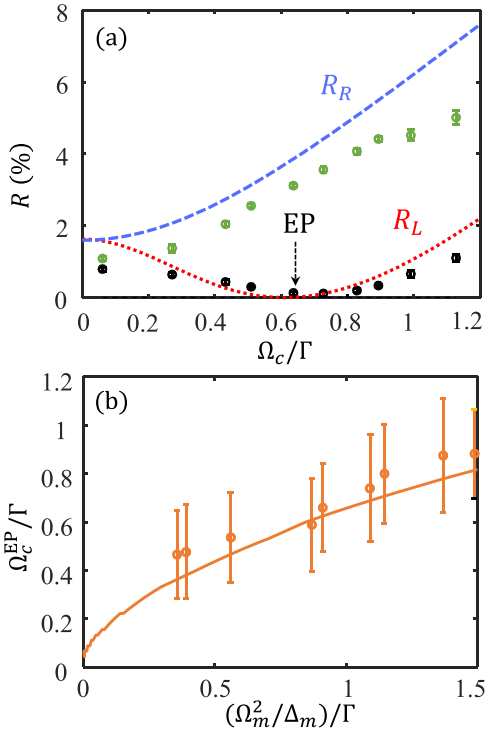

FIG. 6. Experimental observations of the EP and exceptional line. (a) R_L and R_R versus Ω_c for $\phi = \pi/2$ and $\Delta_p = -1.78\Gamma$. The dots are experimental data for R_L (black dots) and R_R (green dots). The error bars are obtained by 10 independent measurements. The red dotted (blue dashed) line represents the numerical simulation for R_L (R_R). The EP is marked at $\Omega_c = 0.65\Gamma$, where $R_L = 0$. (b) Experimental measurement of the exceptional line, i.e., $\Omega_c^{\rm EP}$ versus Ω_m^2/Δ_m. The detunings are kept as $\Delta_p = -2\Omega_m^2/\Delta_m$ and $\Delta_c = -4\Omega_m^2/\Delta_m$. The phase is kept as $\phi = \pi/2$. The experimental results are represented by the dots. The error bars are obtained by 10 independent measurements. The large error bars are due to the insensitivity of R_L on Ω_c near the EP. The solid line is the projection of the intersection line [the white line in Fig. 2(c)] of the two surfaces $\chi_i(\Omega_c, \Omega_m^2/\Delta_m)$ and $\chi_r(\Omega_c, \Omega_m^2/\Delta_m)$ in the plane $(\Omega_c, \Omega_m^2/\Delta_m)$.

ACKNOWLEDGMENTS

We would like to thank J.-H. Wu and Y. Zhang for fruitful discussions. We acknowledge support from the National Natural Science Foundation of China (Grants No. 91736209 and No. 12004334) and the Zhejiang Province Key Research and Development Program (Grant No. 2020C01019).

APPENDIX A: SPATIAL SUSCEPTIBILITY

The Liouville equation of motion for an atom with velocity v along the z axis can be written as [67]

$$\frac{d\rho(v,z,t)}{dt} = -\frac{i}{\hbar}[H_{\rm eff}, \rho(v,z,t)] + L\rho(v,z,t), \tag{A1}$$

where $d/dt = \partial/\partial t + v\partial/\partial z$ and $L\rho$ denotes the additional decay rates and dephasing terms. Substituting $H_{\rm eff}$ into this equation, we obtain the equations of motion for the density matrix elements

$$\frac{d\rho_{22}}{dt} = i2\Omega_c\cos(k_c z)(\rho_{32} - \rho_{23}) + \Gamma_{32}\rho_{33}, \tag{A2a}$$

$$\frac{d\rho_{33}}{dt} = i\Omega_p e^{ik_p z}\rho_{13} - i\Omega_p e^{-ik_p z}\rho_{31} + 2i\Omega_c\cos(k_c z)(\rho_{23} - \rho_{32}) - (\Gamma_{31} + \Gamma_{32})\rho_{33}, \tag{A2b}$$

$$\frac{d\rho_{11}}{dt} = i\Omega_p e^{-ik_p z}\rho_{31} - i\Omega_p e^{ik_p z}\rho_{13} + \Gamma_{31}\rho_{33}, \tag{A2c}$$

$$\frac{d\rho_{23}}{dt} = \{-i[\Delta_c + 2\delta(z,\phi)] - \gamma_{23}\}\rho_{23} - i\Omega_p e^{-ik_p z}\rho_{21} + i2\Omega_c\cos(k_c z)(\rho_{33} - \rho_{22}), \tag{A2d}$$

$$\frac{d\rho_{31}}{dt} = \{i[\Delta_p + \delta(z,\phi)] - \gamma_{31}\}\rho_{31} + i2\Omega_c\cos(k_c z)\rho_{21} - i\Omega_p e^{ik_p z}\rho_{33} + i\Omega_p e^{ik_p z}\rho_{11}, \tag{A2e}$$

$$\frac{d\rho_{21}}{dt} = \{i[\Delta_{pc} - \delta(z,\phi)] - \gamma_{21}\}\rho_{21} + i2\Omega_c\cos(k_c z)\rho_{31} - i\Omega_p e^{ik_p z}\rho_{23}, \tag{A2f}$$

where $\gamma_{31} = (\Gamma_{31} + \Gamma_{32} + \gamma_3)/2$, $\gamma_{21} = \gamma_2/2$, and $\gamma_{23} = (\Gamma_{31} + \Gamma_{32} + \gamma_3 + \gamma_2)/2$ are the decoherence rates. Γ_{ij} is the decay rate from $|i\rangle$ to $|j\rangle$, and γ_i is the dephasing rate of level $|i\rangle$, with $i, j = 1, 2, 3$. The Rabi frequencies Ω_p and Ω_c are both real. In the weak-probe limit $\Omega_p \ll \Omega_c$, we have $\rho_{11} \approx 1$, $\rho_{33} = \rho_{22} = \rho_{23} = 0$. In the steady state ($\partial\rho_{ij}/\partial t = 0$), the relevant equations are

$$v\frac{\partial\rho_{31}}{\partial z} = \{i[\Delta_p + \delta(z,\phi)] - \gamma_{31}\}\rho_{31} + i2\Omega_c\cos(k_c z)\rho_{21} + i\Omega_p e^{ik_p z}, \tag{A3a}$$

$$v\frac{\partial\rho_{21}}{\partial z} = \{i[\Delta_{pc} - \delta(z,\phi)] - \gamma_{21}\}\rho_{21} + i2\Omega_c\cos(k_c z)\rho_{31}. \tag{A3b}$$

To solve these two equations, we expand the density-matrix elements to different Fourier components,

$$\rho_{31}(v,z) = e^{ik_p z}\sum_{n=-\infty}^{+\infty}\rho_{31}^{[n]}(v)e^{-2ink_c z}, \tag{A4a}$$

$$\rho_{21}(v,z) = e^{ik_p z}\sum_{n=-\infty}^{+\infty}\rho_{21}^{[n]}(v)e^{-i(2n+1)k_c z}, \tag{A4b}$$

where $\rho_{31}^{[n]}$ and $\rho_{21}^{[n]}$ are the Fourier coefficients of ρ_{31} and ρ_{21}, with $\partial\rho_{i1}^{[n]}/\partial z = 0, i = 2, 3$. Then we obtain two coupled equations,

$$(\tilde{\Gamma}_{31} + 2ink_c v)\rho_{31}^{[n]} + i\frac{\delta_0}{2}e^{i\phi}\rho_{31}^{[n+1]} + i\frac{\delta_0}{2}e^{-i\phi}\rho_{31}^{[n-1]} + i\Omega_c\rho_{21}^{[n]} + i\Omega_c\rho_{21}^{[n-1]} + i\Omega_p\delta_{n,0} = 0, \tag{A5a}$$

$$[\tilde{\Gamma}_{21} + i(2n+1)k_c v]\rho_{21}^{[n]} - i\frac{\delta_0}{2}e^{i\phi}\rho_{21}^{[n+1]} - i\frac{\delta_0}{2}e^{-i\phi}\rho_{21}^{[n-1]} + i\Omega_c\rho_{31}^{[n]} + i\Omega_c\rho_{31}^{[n+1]} = 0, \tag{A5b}$$

where $\tilde{\Gamma}_{31} = i(\delta_0 + \Delta_p - k_p v) - \gamma_{31}$ and $\tilde{\Gamma}_{21} = i(\Delta_{pc} - \delta_0 - k_p v) - \gamma_{21}.\rho_{31}^{[n]}$ can be solved numerically through the

two equations, where n is truncated at 30 in the numerical calculation. We take $\gamma_{31} = \gamma_{23} = \Gamma$ in the theoretical calculation. The average susceptibility can be expressed as the Doppler integral of the Fourier coefficient ρ_{31} [see Eq. (2) in the main text].

When atoms are static ($v = 0$), the left terms in Eq. (A3) are zero. Then we obtain the analytical expression for the susceptibility,

$$\chi(z) = \frac{\mathcal{N}|\mu_{31}|^2}{\epsilon_0\hbar\Omega_p e^{ik_p z}}\rho_{31} = \frac{\mathcal{N}|\mu_{31}|^2}{\epsilon_0\hbar}\frac{1}{-[\Delta_p + \delta(z,\phi)] - i\gamma_{31} + \frac{4\Omega_c^2\cos(k_c z)}{-[\Delta_{pc} - \delta(z,\phi)] + i\gamma_{21}}}. \tag{A6}$$

This is the standard susceptibility for a standing-wave coupled EIT system, except for the shifted detunings on Δ_p and Δ_{pc} due to the ac Stark shifts of the modulating field. The analytical equation is the same as the numerical simulation (2) in the main text when $v \to 0$.

APPENDIX B: COUPLED-MODE EQUATIONS

The Fourier coefficients χ_{i0}, χ_{r0}, χ_i, and χ_r can be obtained through

$$\chi_{i0} = -\frac{1}{\Lambda}\int_0^\Lambda i\chi(z)dz, \tag{B1a}$$

$$\chi_{r0} = \frac{1}{\Lambda}\int_0^\Lambda \chi(z)dz, \tag{B1b}$$

$$\chi_i = -\frac{2}{\Lambda}\int_0^\Lambda i\chi(z)\cos(2k_c z)dz, \tag{B1c}$$

$$\chi_r = \frac{2}{\Lambda}\int_0^\Lambda \chi(z)\cos(2k_c z + \phi)dz, \tag{B1d}$$

where $\chi(z)$ is given in Eq. (2). These coefficients are used to obtain the analytical expressions of the reflection and transmission coefficients through coupled-mode equations. The eigenmodes in the lattice can be written as $E_p(z) = \mathcal{E}_f(z)e^{ik_p z} + \mathcal{E}_b(z)e^{-ik_p z}$, where $k_p = n_0\omega_p/c$ is the z component of the wave vector of the probe field and $\mathcal{E}_f(z)$ [$\mathcal{E}_b(z)$] denotes the forward (backward) mode in the lattice. $E_p(z)$ obeys the 1D Helmholtz equation

$$\frac{dE_p}{dz} + \frac{\omega_p^2}{c^2}n^2(z)E_p = 0, \tag{B2}$$

where

$$n^2(z) = 1 + \chi \approx 1 + i\chi_{i0} + \chi_{r0} + i\chi_i\cos(2k_c z) + \chi_r\cos(2k_m z + \phi) = n_0^2 + i\chi_{i0} + i\chi_i\cos(2k_c z) + \chi_r\cos(2k_m z + \phi), \tag{B3}$$

with $n_0 = \sqrt{1 + \chi_{r0}}$. Substituting $E_p(z)$ and $n^2(z)$ into the Helmholtz equation, considering the slowly varying approximation ($d^2\mathcal{E}_{f,b}/dz^2 \ll k_p d\mathcal{E}_{f,b}/dz$), we obtain

$$\frac{d\mathcal{E}_f}{dz} = -\frac{k_p\chi_{i0}}{2n_0^2}\mathcal{E}_f + \frac{k_p(i\chi_r e^{i\phi} - \chi_i)}{4n_0^2}\mathcal{E}_b e^{-i\Delta kz}, \tag{B4a}$$

$$\frac{d\mathcal{E}_b}{dz} = \frac{k_p\chi_{i0}}{2n_0^2}\mathcal{E}_b - \frac{k_p(i\chi_r e^{-i\phi} - \chi_i)}{4n_0^2}\mathcal{E}_f e^{i\Delta kz}, \tag{B4b}$$

where $\Delta k = 2k_p - 2k_c$. Using the perfect phase-matching condition $\Delta k = 0$, we obtain the coupled-mode equations

$$\frac{d}{dz}\begin{bmatrix}\mathcal{E}_f \\ \mathcal{E}_b\end{bmatrix} = \frac{k_p}{4n_0^2}\begin{bmatrix}-2\chi_{i0} & \kappa_{b\to f} \\ \kappa_{f\to b} & 2\chi_{i0}\end{bmatrix}\begin{bmatrix}\mathcal{E}_f \\ \mathcal{E}_b\end{bmatrix} = N\begin{bmatrix}\mathcal{E}_f \\ \mathcal{E}_b\end{bmatrix}, \tag{B5}$$

where χ_{i0} denotes the attenuation coefficient of the two modes in the lattice, and the off-diagonal element $\kappa_{b\to f} = i\chi_r e^{i\phi} - \chi_i$ ($\kappa_{f\to b} = -i\chi_r e^{-i\phi} + \chi_i$) denotes the phase-dependent coupling coefficient from the backward (forward) to forward (backward) mode. Then we have

$$\begin{bmatrix}\mathcal{E}_f(z) \\ \mathcal{E}_b(z)\end{bmatrix} = e^{Nz}\begin{bmatrix}\mathcal{E}_f(0) \\ \mathcal{E}_b(0)\end{bmatrix} = M(z)\begin{bmatrix}\mathcal{E}_f(0) \\ \mathcal{E}_b(0)\end{bmatrix}, \tag{B6}$$

where $M(z)$ is the transfer matrix and can be written in 2×2 matrix form,

$$M(z) = \begin{bmatrix}M_{11}(z) & M_{12}(z) \\ M_{21}(z) & M_{22}(z)\end{bmatrix}. \tag{B7}$$

The four matrix elements are

$$M_{11}(z) = \cosh(\xi z) - \frac{k_p\chi_{i0}}{2n_0^2\xi}\sinh(\xi z), \tag{B8a}$$

$$M_{12}(z) = \frac{k_p\kappa_{b\to f}}{4n_0^2\xi}\sinh(\xi z), \tag{B8b}$$

$$M_{21}(z) = \frac{k_p\kappa_{f\to b}}{4n_0^2\xi}\sinh(\xi z), \tag{B8c}$$

$$M_{22}(z) = \cosh(\xi z) + \frac{k_p\chi_{i0}}{2n_0^2\xi}\sinh(\xi z), \tag{B8d}$$

where $\xi = (k_p/4n_0^2)\sqrt{4\chi_{i0}^2 - \chi_i^2 + \chi_r^2 + 2i\chi_i\chi_r\cos\phi}$. With the boundary conditions $\mathcal{E}_f(0) = \mathcal{E}_0$, $\mathcal{E}_b(L) = 0$ and $\mathcal{E}_b(L) = \mathcal{E}_0$, $\mathcal{E}_f(0) = 0$, we can obtain the reflection and transmission coefficients

$$r_L = -\frac{M_{21}(L)}{M_{22}(L)} = -\frac{(\chi_i - i\chi_r\cos\phi - \chi_r\sin\phi)\sinh(\xi L)}{(4n_0^2\xi/k_p)\cosh(\xi L) + 2\chi_{i0}\sinh(\xi L)}, \tag{B9a}$$

$$r_R = \frac{M_{12}(L)}{M_{22}(L)} = -\frac{(\chi_i - i\chi_r\cos\phi + \chi_r\sin\phi)\sinh(\xi L)}{(4n_0^2\xi/k_p)\cosh(\xi L) + 2\chi_{i0}\sinh(\xi L)}, \tag{B9b}$$

$$t_L = t_R = t = \frac{1}{M_{22}(L)} = \frac{2n_0^2\xi}{2n_0^2\xi\cosh(\xi L) + k_p\chi_{i0}\sinh(\xi L)}. \tag{B9c}$$

The unidirectional reflectionless propagation can also be understood from the unidirectional coupling. When $\phi = 0$ and

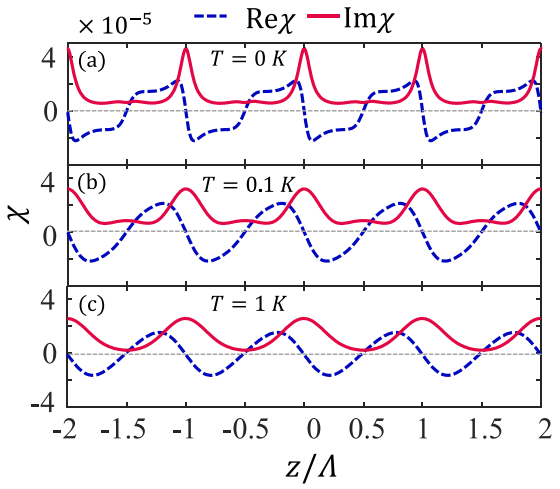

FIG. 7. The anti-PT-symmetric susceptibility for different temperatures T. (a) $T = 0$ K. (b) $T = 0.1$ K. (c) $T = 1$ K. Other parameters are the same as in Fig. 2(a) in the main text.

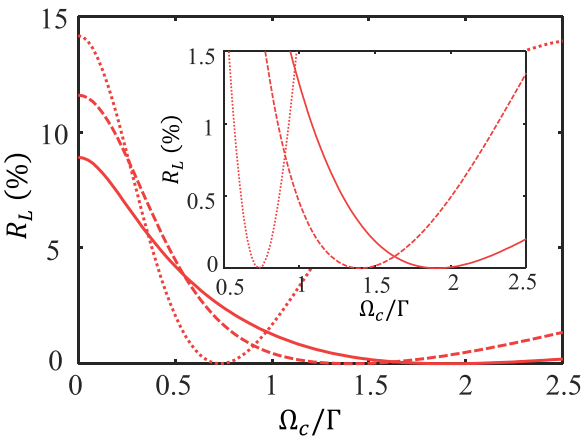

FIG. 8. The reflectivity R_L versus Ω_c for different temperatures. $T = 0$ K (solid line), $T = 0.1$ K (dashed line), and $T = 1$ K (dotted line). The inset highlights zero points of R_L. EPs are $\Omega_c^{\mathrm{EP}} = 1.92\Gamma$ ($T = 0$ K), 1.41Γ ($T = 0.1$ K), and 0.73Γ ($T = 1$ K).

$\phi = \pi$, we have $|\kappa_{b\to f}| = |\kappa_{f\to b}|$. In this case, we have symmetric reflections ($r_L = r_R$). When $\phi \neq 0$ or π, the coupling coefficients are different, i.e., $\kappa_{b\to f} \neq \kappa_{f\to b}$, which leads to asymmetric reflections ($r_L \neq r_R$). Interestingly, at the anti-PT symmetric condition $\phi = \pi/2$, the coupling coefficients are $\kappa_{b\to f} = -\chi_r - \chi_i$ and $\kappa_{f\to b} = \chi_i - \chi_r$, respectively. The unidirectional coupling occurs at $\chi_i = \chi_r$, where $\kappa_{f\to b} = 0$ and $\kappa_{b\to f} \neq 0$. Therefore, the unidirectional coupling leads to the unidirectional reflectionless propagation for the forward probe field ($r_L = 0$ and $r_R \neq 0$). In the same way, at $\phi = 3\pi/2$, the unidirectional coupling ($\kappa_{b\to f} = 0$ and $\kappa_{f\to b} \neq 0$) leads to the unidirectional reflectionless propagation for the backward probe field ($r_R = 0$ and $r_L \neq 0$).

APPENDIX C: THE EFFECT OF DOPPLER BROADENING

The Doppler broadening plays an important role in this system due to the thermal atomic motion. To investigate the effect of Doppler broadening, we calculate the spatial susceptibility for different temperatures, which determine the widths of Doppler broadening. Meanwhile, we assume the atomic density is invariant. In Fig. 7, we plot the spatial susceptibilities for three different temperatures ($T = 0$ K, $T = 0.1$ K, $T = 1$ K), where probe detuning and phase are kept at $\Delta_p = -1.78\Gamma$ and $\phi = \pi/2$. The widths of Doppler broadening $k_c u$ are 0, 0.86Γ, and 2.7Γ, respectively. With the increasing temperature (i.e., Doppler broadening), the modulation of the susceptibility becomes smaller, and the profile becomes smoother. This property has been analyzed in [67]. When we increase the temperature from 1 K to room temperature, the modulation amplitude decreases, and the profile almost does not change [see Fig. 2(a)].

It can be seen that the Doppler broadening changes the amplitudes of the susceptibility but not the symmetry of the lattice. In other words, the anti-PT-symmetric susceptibility $\chi(z) = -\chi^*(-z)$ is independent of the Doppler broadening. Actually, it is the spatial phase difference $\phi = \pi/2$ (or $3\pi/2$) between the two standing-wave fields that determines the anti-PT symmetry of the lattice. In addition, the anti-PT symmetry does not depend on the choice of $z = 0$ either. We can choose $z = \pm 0.5\Lambda$ as the zero point, where the relation $\chi(z) = -\chi^*(-z)$ is also satisfied.

Due to the changes in the susceptibility under the Doppler broadening, the EP may be different. To show the influence of Doppler broadening on the EP, we plot the reflectivity R_L versus Ω_c for different temperatures with $\Delta_p = -1.78\Gamma$ and $\phi = \pi/2$ in Fig. 8. We can see that the EP changes with the temperature. The EPs are $\Omega_c^{\mathrm{EP}} = 1.92\Gamma$ ($T = 0$ K), 1.41Γ ($T = 0.1$ K), and 0.73Γ ($T = 1$ K), respectively. Therefore, Ω_c^{EP} decreases with the increase of the Doppler broadening.

In summary, the Doppler broadening changes the amplitude of the spatial susceptibility and the EP, but it does not affect the anti-PT symmetry of the susceptibility. Therefore, the anti-PT-symmetric photonic lattice can also be realized in homogeneous cold atoms, and the unidirectional reflectionless light propagation can be observed.

[1] L. Feng, R. El-Ganainy, and L. Ge, Non-Hermitian photonics based on parity-time symmetry, Nat. Photonics **11**, 752 (2017).

[2] R. El-Ganainy, K. G. Makris, M. Khajavikhan, Z. H. Musslimani, S. Rotter, and D. N. Christodoulides, Non-Hermitian physics and PT symmetry, Nat. Phys. **14**, 11 (2018).

[3] Ş. K. Özdemir, S. Rotter, F. Nori, and L. Yang, Parity–time symmetry and exceptional points in photonics, Nat. Mater. **18**, 783 (2019).

[4] A. Guo, G. J. Salamo, D. Duchesne, R. Morandotti, M. Volatier-Ravat, V. Aimez, G. A. Siviloglou, and D. N. Christodoulides, Observation of PT-Symmetry Breaking in

Complex Optical Potentials, Phys. Rev. Lett. **103**, 093902 (2009).

[5] C. E. Rüter, K. G. Makris, R. El-Ganainy, D. N. Christodoulides, M. Segev, and D. Kip, Observation of parity-time symmetry in optics, Nat. Phys. **6**, 192 (2010).

[6] A. Regensburger, C. Bersch, M.-A. Miri, G. Onishchukov, D. N. Christodoulides, and U. Peschel, Parity-time synthetic photonic lattices, Nature (London) **488**, 167 (2012).

[7] B. Peng, Ş. K. Özdemir, F. Lei, F. Monifi, M. Gianfreda, G. L. Long, S. Fan, F. Nori, C. M. Bender, and L. Yang, Parity-time-symmetric whispering-gallery microcavities, Nat. Phys. **10**, 394 (2014).

[8] L. Chang, X. Jiang, S. Hua, C. Yang, J. Wen, L. Jiang, G. Li, G. Wang, and M. Xiao, Parity-time symmetry and variable optical isolation in active-passive-coupled microresonators, Nat. Photonics **8**, 524 (2014).

[9] Z. J. Wong, Y.-L. Xu, J. Kim, K. O'Brien, Y. Wang, L. Feng, and X. Zhang, Lasing and anti-lasing in a single cavity, Nat. Photonics **10**, 796 (2016).

[10] Z. Lin, H. Ramezani, T. Eichelkraut, T. Kottos, H. Cao, and D. N. Christodoulides, Unidirectional Invisibility Induced by $\mathcal{PT}$-Symmetric Periodic Structures, Phys. Rev. Lett. **106**, 213901 (2011).

[11] L. Feng, Y.-L. Xu, W. S. Fegadolli, M.-H. Lu, J. E. Oliveira, V. R. Almeida, Y.-F. Chen, and A. Scherer, Experimental demonstration of a unidirectional reflectionless parity-time metamaterial at optical frequencies, Nat. Mater. **12**, 108 (2013).

[12] Y. D. Chong, L. Ge, and A. D. Stone, $\mathcal{PT}$-Symmetry Breaking and Laser-Absorber Modes in Optical Scattering Systems, Phys. Rev. Lett. **106**, 093902 (2011).

[13] L. Ge, Y. D. Chong, and A. D. Stone, Conservation relations and anisotropic transmission resonances in one-dimensional $\mathcal{PT}$-symmetric photonic heterostructures, Phys. Rev. A **85**, 023802 (2012).

[14] X. Zhu, H. Ramezani, C. Shi, J. Zhu, and X. Zhang, $\mathcal{PT}$-Symmetric Acoustics, Phys. Rev. X **4**, 031042 (2014).

[15] R. Fleury, D. Sounas, and A. Alù, An invisible acoustic sensor based on parity-time symmetry, Nat. Commun. **6**, 5905 (2015)

[16] C. Z. Shi, M. Dubois, Y. Cheng, H. Ramezani, Y. Wang, and X. Zhang, Accessing the exceptional points of parity-time symmetric acoustics, Nat. Commun. **7**, 11110 (2016)

[17] T. Liu, X. F. Zhu, F. Chen, S. J. Liang, and J. Zhu, Unidirectional Wave Vector Manipulation in Two-Dimensional Space with an All Passive Acoustic Parity-Time-Symmetric Metamaterials Crystal, Phys. Rev. Lett. **120**, 124502 (2018).

[18] H. Hodaei, A. U. Hassan, S. Wittek, H. G. Gracia, R. El-Ganainy, D. N. Christodoulides, and M. Khajavikhan, Enhanced sensitivity at higher-order exceptional points, Nature (London) **548**, 187 (2017)

[19] W. J. Chen, Ş. K. Özdemir, G. M. Zhao, J. Wiersig, and L. Yang, Exceptional points enhance sensing in an optical microcavity, Nature (London) **548**, 192 (2017)

[20] Z. C. Xiao, H. N. Li, T. Kottos, and A. Alù, Enhanced Sensing and Nondegraded Thermal Noise Performance Based on PT Symmetric Electronic Circuits with a Sixth-Order Exceptional Point, Phys. Rev. Lett. **123**, 213901 (2019).

[21] M. Z. Zhang, W. Sweeney, C. W. Hsu, L. Yang, A. D. Stone, and L. Jiang, Quantum Noise Theory of Exceptional Point Amplifying Sensors, Phys. Rev. Lett. **123**, 180501 (2019).

[22] S. Yu, Y. Meng, J. S. Tang, X. Y. Xu, Y. T. Wang, P. Yin, Z. J. Ke, W. Liu, Z. P. Li, Y. Z. Yang, G. Chen, Y. J. Han, C. F. Li, and G. C. Guo, Experimental Investigation of Quantum $\mathcal{PT}$-Enhanced Sensor, Phys. Rev. Lett. **125**, 240506 (2020).

[23] L. Y. Ding, K. Y. Shi, Q. X. Zhang, D. N. Shen, X. Zhang, and W. Zhang, Experimental Determination of $\mathcal{PT}$-symmetric Exceptional Points in a Single Trapped Ion, Phys. Rev. Lett. **126**, 083604 (2021).

[24] B. Peng, Ş. K. Özdemir, M. Liertzer, W. J. Chen, J. Kramer, H. Yı lmaz, J. Wiersig, S. Rotter, and L. Yang, Chiral modes and directional lasing at exceptional points, Proc. Natl. Acad. Sci. USA **113**, 6845 (2016).

[25] J. Doppler, A. A. Mailybaev, J. Böhm, U. Kuhl, A. Girschik, F. Libisch, T. J. Milburn, P. Rabl, N. Moiseyev, and S. Rotter, Dynamically encircling an exceptional point for asymmetric mode switching, Nature (London) **537**, 76 (2016).

[26] H. Xu, D. Mason, L. Jiang, and J. G. E. Harris, Topological energy transfer in an optomechanical system with exceptional points, Nature (London) **537**, 80 (2016).

[27] P. Peng, W. Cao, C. Shen, W. Qu, J. Wen, L. Jiang, and Y. Xiao, Anti-parity-time symmetry with flying atoms, Nat. Phys. **12**, 1139 (2016).

[28] F. Yang, Y.-C. Liu, and L. You, Anti-$\mathcal{PT}$ symmetry in dissipatively coupled optical systems, Phys. Rev. A **96**, 053845 (2017).

[29] V. V. Konotop and D. A. Zezyulin, Odd-Time Reversal $\mathcal{PT}$ Symmetry Induced by an Anti-$\mathcal{PT}$-Symmetric Medium, Phys. Rev. Lett. **120**, 123902 (2018).

[30] Q. Li, C. J. Zhang, Z. D. Cheng, W. Z. Liu, J. F. Wang, F. F. Yan, Z. H. Lin, Y. Xiao, K. Sun, Y. T. Wang, J. S. Tang, J. S. Xu, C. F. Li, and G. C. Guo, Experimental simulation of anti-parity-time symmetric Lorentz dynamics, Optica **6**, 67 (2019).

[31] Y. Choi, C. Hahn, J. W. Yoon, and S. H. Song, Observation of an anti-PT-symmetric exceptional point and energy-difference conserving dynamics in electrical circuit resonators, Nat. Commun. **9**, 2182 (2018).

[32] X.-L. Zhang, T. Jiang, and C. T. Chan, Dynamically encircling an exceptional point in anti-parity-time symmetric systems: Asymmetric mode switching for symmetry-broken modes, Light: Sci. Appl. **8**, 1 (2019).

[33] Y. Li, Y.-G. Peng, L. Han, M.-A. Miri, W. Li, M. Xiao, X.-F. Zhu, J. Zhao, A. Alù, S. Fan, and C.-W. Qiu, Anti-parity-time symmetry in diffusive systems, Science **364**, 170 (2019).

[34] Y. Yang, Y. P. Wang, J. W. Rao, Y. S. Gui, B. M. Yao, W. Lu, and C. M. Hu, Unconventional Singularity in Anti-Parity-Time Symmetric Cavity Magnonics, Phys. Rev. Lett. **125**, 147202 (2020).

[35] H. L. Zhang, R. Huang, S. D. Zhang, Y. Li, C. W. Qiu, F. Nori, and H. Jing, Breaking anti-PT symmetry by spinning a resonator, Nano Lett. **20**, 7594 (2020).

[36] H. Fan, J. Y. Chen, Z. T. Zhao, J. M. Wen, and Y. P. Huang, Antiparity-time symmetry in passive nanophotonics, ACS Photonics **7**, 3035 (2020)

[37] A. Bergman, R. Duggan, K. Sharma, M. Tur, A. Zadok, and A. Alù, Observation of anti-parity-time-symmetry, phase transitions and exceptional points in an optical fibre, Nat. Commun. **12**, 486 (2021)

[38] J. M. P. Nair, D. Mukhopadhyay, and G. S. Agarwal, Enhanced Sensing of Weak Anharmonicities through Coherences in Dissipatively Coupled Anti-$\mathcal{PT}$ Symmetric Systems, Phys. Rev. Lett. **126**, 180401 (2021).

[39] Y. Jiang, Y. Mei, Y. Zuo, Y. Zhai, J. Li, J. Wen, and S. Du, Anti-Parity-Time Symmetric Optical Four-Wave Mixing in Cold Atoms, Phys. Rev. Lett. **123**, 193604 (2019).

[40] F. X. Zhang, Y. M. Feng, X. F. Chen, L. Ge, and W. J. Wan, Synthetic Anti-$\mathcal{PT}$ Symmetry in a Single Microcavity, Phys. Rev. Lett. **124**, 053901 (2020).

[41] S. Park, D. Lee, K. Park, H. Shin, Y. Choi, and J. W. Yoon, Optical Energy-Difference Conservation in a Synthetic Anti-PT-Symmetric System, Phys. Rev. Lett. **127**, 083601 (2021).

[42] L. Ge and H. E. Türeci, Antisymmetric $\mathcal{PT}$-photonic structures with balanced positive-and negative-index materials, Phys. Rev. A **88**, 053810 (2013).

[43] J.-H. Wu, M. Artoni, and G. C. La Rocca, Non-Hermitian Degeneracies and Unidirectional Reflectionless Atomic Lattices, Phys. Rev. Lett. **113**, 123004 (2014).

[44] J.-H. Wu, M. Artoni, and G. C. Rocca, Parity-time-antisymmetric atomic lattices without gain, Phys. Rev. A **91**, 033811 (2015).

[45] X. Wang, J.-H. Wu, Optical PT-symmetry and PT-antisymmetry in coherently driven atomic lattices, Opt. Express **24**, 4289 (2016).

[46] Y.-L. Chuang, Ziauddin, and R.-K. Lee, Realization of simultaneously parity-time-symmetric and parity-time-antisymmetric susceptibilities along the longitudinal direction in atomic systems with all optical controls, Opt. Express **26**, 21969 (2018).

[47] Y.-L. Chuang, A. Shamsi, M. Abbas, and Ziauddin, Coherent control of nonreciprocal reflections with spatial modulation coupling in parity-time symmetric atomic lattice, Opt. Express **28**, 1701 (2020).

[48] M. Fleischhauer, A. Imamoglu, and J. P. Marangos, Electromagnetically induced transparency: Optics in coherent media, Rev. Mod. Phys. **77**, 633 (2005).

[49] M. Bajcsy, A. S. Zibrov, and M. D. Lukin, Stationary pulses of light in an atomic medium, Nature (London) **426**, 638 (2003).

[50] J.-X. Zhang, H.-T. Zhou, D.-W. Wang, and S.-Y. Zhu, Enhanced reflection via phase compensation from anomalous dispersion in atomic vapor, Phys. Rev. A **83**, 053841 (2011).

[51] D.-W. Wang, H.-T. Zhou, M.-J. Guo, J.-X. Zhang, J. Evers, and S.-Y. Zhu, Optical Diode Made from a Moving Photonic Crystal, Phys. Rev. Lett. **110**, 093901 (2013).

[52] A. M. Brown and M. Xiao, All-optical switching and routing based on an electromagnetically induced absorption grating, Opt. Lett. **30**, 699 (2005).

[53] Z. Y. Zhang, D. M. Ma, Y. Q. Yi, M. T. Cao, Z. F. Xu, and Y. P. Zhang, Propagation of optical vortices in a nonlinear atomic medium with a photonic band gap, Opt. Lett. **42**, 1059 (2017).

[54] Z. Y. Zhang, Y. T. Shen, S. H. Ning, S. Liang, Y. Feng, C. B. Li, Y. P. Zhang, and M. Xiao, Transport of light in a moving photonic lattice via atomic coherence, Opt. Lett. **46**, 4096 (2021).

[55] Z. Y. Zhang, Y. Q. Zhang, J. T. Sheng, L. Yang, M. A. Miri, D. N. Christodoulides, B. He, Y. P. Zhang, and M. Xiao, Observation of Parity-Time Symmetry in Optically Induced Atomic Lattices, Phys. Rev. Lett. **117**, 123601 (2016).

[56] H. Cai, J. Liu, J. Wu, Y. He, S.-Y. Zhu, J.-X. Zhang, and D.-W. Wang, Experimental Observation of Momentum-Space Chiral Edge Currents in Room-Temperature Atoms, Phys. Rev. Lett. **122**, 023601 (2019).

[57] Y. X. Yan and N. C. Giebink, Passive PT symmetry in organic composite films via complex refractive index modulation, Adv. Opt. Mater. **2**, 423 (2014).

[58] Y. F. Jia, Y. X. Yan, S. V. Kesava, E. D. Gomez, and N. C. Giebink, Passive parity-time symmetry in organic thin film waveguides, ACS Photonics **2**, 319 (2015).

[59] C. Hahn, Y. Choi, J. W. Yoon, S. H. Song, C. H. Oh, and P. Berini, Observation of exceptional points in reconfigurable non-Hermitian vector-field holographic lattices, Nat. Commun. **7**, 12201 (2016).

[60] A. Mostafazadeh, Pseudo-Hermiticity versus PT symmetry: The necessary condition for the reality of the spectrum of a non-Hermitian Hamiltonian, J. Math. Phys. (Melville, NY, US) **43**, 205 (2002).

[61] M. Artoni, G. La Rocca, and F. Bassani, Resonantly absorbing one-dimensional photonic crystals, Phys. Rev. E **72**, 046604 (2005).

[62] X. Zhang, K. Ding, X. Zhou, J. Xu, and D. Jin, Experimental Observation of an Exceptional Surface in Synthetic Dimensions with Magnon Polaritons, Phys. Rev. Lett. **123**, 237202 (2019)

[63] D. G. Baranov, A. Krasnok, T. Shegai, A. Alù, and Y. D. Chong, Coherent perfect absorbers: linear control of light with light, Nat. Rev. Mater. **2**, 17064 (2017)

[64] T. Shui, W. X. Yang, L. Li, and X. Wang, Lop-sided Raman–Nath diffraction in PT-antisymmetric atomic lattices, Opt. Lett. **44**, 2089 (2019).

[65] J. B. Khurgin, Y. Sebbag, E. Edrei, R. Zektzerm, K. Shastri, U. Levy, and F. Monticone, Emulating exceptional-point encirclements using imperfect (leaky) photonic components: asymmetric mode-switching and omni-polarizer action, Optica **8**, 563 (2021).

[66] Y. He, R. Mao, H. Cai, J.-X. Zhang, Y. Li, L. Yuan, S.-Y. Zhu, and D.-W. Wang, Flat-Band Localization in Creutz Superradiance Lattices, Phys. Rev. Lett. **126**, 103601 (2021).

[67] S. Q. Kuang, R. G. Wan, P. Du, Y. Jiang, and J. Y. Gao, Transmission and reflection of electromagnetically induced absorption grating in homogeneous atomic media, Opt. Express **16**, 15455 (2008).